SPHERULITIC MORPHOLOGIES OF THE TRIBLOCK POLY(GL)-*b*-POLY(GL-*co*-TMC-*co*-CL)-*b*-POLY(GL) COPOLYMER: ISOTHERMAL AND NON-ISOTHERMAL

Yolanda Márquez[1], Lourdes Franco[1], Juan Carlos Martínez,[3] Francesc Estrany[1], Pau Turon[2], Jordi Puiggalí[1*]

[1]Departament d'Enginyeria Química, Universitat Politècnica de Catalunya, Av. Diagonal 647, Barcelona E-08028, SPAIN

[2]B. Braun Surgical S.A., Carretera de Terrasa 121, Rubí (Barcelona), 08191, SPAIN

[3]ALBA Synchrotron Light Facility, Ctra. BP 1413 km. 3.3, 08290 Cerdanyola del Vallès, Barcelona , SPAIN (**www.albasynchrotron.es**)

Correspondence to: **J. Puiggalí (Phone: 34-934015649, E-mail: Jordi.Puiggali@upc.edu)**

ABSTRACT

Crystallization of a biodegradable segmented copolymer constituted by polyglycolide hard segments and a middle soft segment constituted by a random disposition of glycolyl, ε-caproyl and trimethylene carbonyl units has been studied by means of optical microscopy, atomic force microscopy and time resolved X-ray diffraction techniques. This GL-*b*-(GL-*co*-TMC-*co*-CL)-*b*-GL copolymer is widely employed as surgical suture and has similar characteristics than previously studied copolymers having a middle soft segment constituted by only two monomers (i.e. glycolide and trimethylene carbonate).

FTIR and NMR spectroscopies demonstrated that the middle segment had an amorphous character and a random microstructure as consequence of transesterification reactions that took place during synthesis. Nevertheless, polyglycolide segments were able to crystallize giving rise to peculiar positive birefringent spherulites with a morphology, which depends on crystallization temperature (i.e. flat-on and edge-on crystals) as verified by AFM and electron diffraction patterns.

Complete bell shaped curves that defined the temperature dependence of the crystal growth rate could be experimentally obtained from both, isothermal and non-isothermal crystallizations. Data from both analyses were in close agreement and pointed out a secondary nucleation constant (2.42-*2*.88 × 10^5 K^2) which was clearly higher than that determined for the related system with two components. Lamellar morphologic parameters were similar for samples crystallized from the melt state and after the reordering process that took place on heating. Comparing to the bicomponent system, significant differences were again observed highlighting the influence of the soft segment on the crystallization behaviour.

Keywords: Absorbable sutures, glycolide copolymer, crystallization kinetics, isothermal crystallization, non-isothermal crystallization, spherulitic morphology.

INTRODUCTION

Polyglycolide is a biodegradable polyester widely employed for biomedical applications, being specifically the development of bioabsorbable surgical sutures one of its first applications.[1-8] Polyglycolide has a distinctive crystalline structure that renders differentiated properties respect to similar aliphatic polyesters.[9] Thus, for example it has a melting temperature higher than 200 ºC and a glass transition temperature in the 35-40 °C range that contrast with the low values found for the other members of the series (e.g. melting point of 55–60 °C and glass transition temperature close to –60 °C for poly(ε-caprolactone)[10]). In addition, polyglycolide is relatively hygroscopic and therefore exhibits a high degradation rate, shows a good biocompatibility and excellent fiber forming properties. These good properties can be extended to a wide range of copolymers differing on components and composition, being specifically degradation behavior and mechanical properties intensively investigated.[11-15]

Bioabsorbable surgical sutures can be processed in monofilament and multifilament forms, being the former preferred due to advantages like more resistance to harbor microorganisms and higher facility to passage through tissue than conventional braided threads.[16-18] The high stiffness of polyglycolide makes its processing as a monofilament suture impossible, being therefore different formulations developed to get flexible materials while glycolide is kept as a predominant component. In this way, different segmented copolymers having two polyglycolide hard segments and a middle soft segment derived from glycolide and other monomers (e.g. trimethylene carbonate, ε-caprolactone or *p*-dioxanone) have been prepared to provide flexibility.[19-21]

Maxon™ (Syneture) is one of the most simple monofilament synthetic sutures based on glycolide copolymers that has been employed. This copolymer is characterized by a 62

wt-% of polyglycolide hard segments and a middle soft segment constituted by a random disposition of 85 wt-% of trimethylene carbonate and 15 wt-% of glycolide.[22] The design of this poly(GL)-*b*-poly(GL-*co*-TMC)-*b*-poly(GL) copolymer is relevant to meet the requirements of a bioresorbable suture. It should be also considered that processing affects crystallinity and hence mechanical properties and degradability. In this way, comprehension of the crystallization process in a polymeric system where amorphous (soft segments) and crystalline domains (hard segments) coexist is a highly interesting topic.

The crystallization process of poly(GL)-*b*-poly(GL-*co*-TMC)-*b*-poly(GL) has been extensively evaluated under both isothermal and non-isothermal conditions for the commercial sample[23,24] as well as for copolymers with slightly different microstructure. Results demonstrated that small variations on the hard segment length and the soft segment content had a high influence on melting temperature, degree of crystallinity, degradation rate, crystallization kinetics and crystalline morphology.[25-27] For example, the crystalline lamellar thickness is higher for samples with a low polyglycolide hard segment content as a consequence of the incorporation of soft segments into the crystalline phase in such a way that imperfect crystals with a low melting point are developed.[27]

Poly(GL)-*b*-poly(GL-*co*-TMC-*co*-CL)-*b*-poly(GL) has also been employed as a monofilament suture with properties (e.g. in vitro degradation) that covers a similar range than Maxon™. This segmented copolymer is synthesized following a two step procedure (Figure S1 in Supporting information (SI)), which renders a middle soft segment based on three components and two polyglycolide hard blocks.[20] With regard to Maxon™, it is significant the different constitution of the soft segment (three components instead of two),

the lower hard segment percentage (57 versus 62 wt-%) and the slightly higher glycolyl content (72 versus 67.5 wt-%).

Studies about the crystallization process of the commercial poly(GL)-*b*-poly(GL-*co*-TMC-*co*-CL)-*b*-poly(GL) suture are scarce and basically concern to isothermal and non-isothermal analyses from DSC calorimetric data.[28] These indicated a maximum overall crystallization rate around 131 °C and a secondary nucleation constant of 1.51×10^5 K^2 that became lower than reported for Maxon™ (1.86×10^5 K^2). This is an expected result taking into account the higher content of non-crystallizable soft segments with greater statistical monomer distribution. Therefore, a complementary study using optical microscopy data appears necessary. Furthermore, morphologic data concerning the lamellar structure are also interesting in order to improve comprehension of how small changes on the polymer architecture can affect microphase separation. In fact, fiber properties are governed by physical structures of different scales, including amorphous and crystalline domains as well as lamellar structures.

EXPERIMENTAL SECTION

Materials

Commercially available sutures of GL-*b*-(GL-*co*-TMC-*co*-CL)-*b*-GL (Monosyn™, USP 1) were kindly supplied by B. Braun Surgical, S.A. This triblock copolymer has a middle soft segment that constitutes a 43 wt-% of the sample and that is composed of 35 wt-%, 32.5 wt-% and 32.5 wt-% of glycolyl, trimethylene carbonyl and ε-caproyl units, respectively.[20] Diethylene glycol was used as a bifunctional initiator for the ring opening polymerization that leads to the soft segment (see the first synthesis step of Figure S1 in SI). Therefore, a prepolymer having two hydroxyl terminal groups was obtained and consequently polyglycolide hard blocks could be incorporated at both

ends in the second polymerization step (Figure S1 in SI). Weight and number average molecular weights of GL-*b*-(GL-*co*-TMC-*co*-CL)-*b*-GL samples were 71,000 and 41,000 g/mol, as previously reported.[28]

Measurements

^{1}H-NMR spectra were acquired with a Bruker AMX-300 spectrometer operating at 300.1 MHz. Chemical shifts were calibrated using tetramethylsilane as an internal standard. Dried dimethyl sulfoxide-d_6 (DMSO) was used as the solvent at a temperature of 90-95 ºC to enhance solubility and resolution.

Infrared absorption spectra were recorded with a Fourier Transform FTIR 4100 Jasco spectrometer in the 4000-600 cm^{-1} range. A Specac model MKII Golden Gate attenuated total reflection (ATR) cell with a heated Diamond ATR Top-Plate which can be used at up to 200 ºC, and a Series 4000 High Stability Temperature Controler were also employed.

Calorimetric data were obtained by differential scanning calorimetry with a TA Instruments Q100 series. Experiments were conducted under a flow of dry nitrogen with a sample weight of approximately 5 mg and at a heating rate of 20 ºC/min.

The spherulite growth rate was determined by optical microscopy using a Zeiss Axioskop 40 Pol light polarizing microscope equipped with a Linkam temperature control system configured by a THMS 600 heating and freezing stage connected to a LNP 94 liquid nitrogen cooling system. Spherulites were grown from homogeneous thin films prepared by evaporation of dilute solutions of the polymer in 1,1,1,3,3,3-hexafluoroisopropanol (0.5 mg/mL). Next, small sections of these films were pressed or smeared between two cover slides and inserted into the hot stage, with thicknesses of close to 10 μm in all cases. Samples were kept at 220 ºC (approximately 20 ºC above the polymer melting point of 200 ºC) for 5 minutes to eliminate sample history effects.

For hot crystallization experiments, samples were quickly cooled to the selected crystallization temperature for cold crystallization experiments, they were quickly cooled to room temperature and then quickly heated to the selected crystallization temperature. The radius of growing spherulites was monitored during crystallization with micrographs taken with a Zeiss AxiosCam MRC5 digital camera at appropriate time intervals. A first-order red tint plate was employed to determine the sign of spherulite birefringence under crossed polarizers. For non-isothermal experiments the radius of growing spherulites was also monitored during crystallization with micrographs taken at appropriate time intervals.

A Philips TECNAI 10 electron microscope was used and operated at 100 kV for bright field and electron diffraction modes, respectively. Selected area electron diffraction patterns were taken with a SIS MegaView II digital camera and internally calibrated with gold (d_{111} = 0.235 nm). Spherulites were grown at 80 and 150 ºC from melted thin films which had previously been prepared by solvent casting from a dilute solution of the polymer in 1,1,1,3,3,3-hexafluoroisopropanol. Nucleation density was determined from low magnification micrographs (i.e. ×100 due to the great size of spherulites) by counting the number of spherulites developed in representative areas (e.g. Figure S2 in SI).

For AFM studies, thin films were prepared by solvent casting of a dilute solution in 1,1,1,3,3,3-hexafluoroisopropanol and placed between cover slides. Samples were subsequently heated above the melting point to perform cold (after quenching) and hot crystallization experiments at the selected temperatures. After crystallization cover slides were manually separated to perform AFM observations. This feature caused some limitations on the image quality and especially for the thinnest spherulites characterized by a planar lamellar disposition as then will be shown. Height and amplitude images of spherulites were obtained with a Molecular Imaging PicoSPM using a NanoScope IV

controller in ambient conditions and a scan window size of 10 x 10 μm^2. The tapping mode AFM was operated at constant deflections (i.e. vertical constant force with triangular gold-coated silicon nitride). Row scanning frequency was set to 1 Hz and physical tip-sample motion speed was 10 μm/s.

Time resolved SAXS experiments were carried out at the NCD beamline (BL11) of the Alba synchrotron radiation light facility of Cerdanyola del Vallès (Catalunya). The beam was monochromatized to a wavelength of 0.100 nm. Polymer samples were confined in capillaries and then held on a Linkam HFSX-350-CAP hot stage with temperature control within ± 0.1 ºC. SAXS profiles were acquired during heating and cooling runs in time frames of 20 s and rates of 10 ºC/min. The detector was calibrated with different orders of diffraction from silver behenate. The diffraction profiles were normalized to the beam intensity and corrected considering the empty sample background. The correlation function and corresponding parameters were calculated with the CORFUNC program for Fibre Diffraction / Non-Crystalline Diffraction provided by the Collaborative Computational Project 13. The WAXD detector was calibrated with diffractions of a standard of a Cr_2O_3 sample. The diffraction profiles were normalized to the beam intensity and corrected considering the empty sample background. Deconvolution of WAXD peaks was performed with the PeakFit v4 program by Jandel Scientific Software using a mathematical function known as "Gaussian area".

RESULTS AND DISCUSSION

Characterization of GL-*b*-(GL-*co*-TMC-*co*-CL)-*b*-GL

Figure 1 shows the ^{1}H-NMR spectra of the GL-*b*-(GL-*co*-TMC-*co*-CL)-*b*-GL sample with an assignment of the characteristic signals based on previous works on bicomponent systems (i.e. poly(glycolide-*co*-trimethylene carbonate)[29] and poly(glycolide-*co*-

caprolactone)[30]). A sequence sensitivity is observed, especially for signals corresponding to glycolyl protons, which extends over the 4.83-4.57 ppm range (Table S1 of SI and inset of Figure 2). It is interesting to remark that the signal of the middle glycolyl protons of a G*G*G sequence (G, glycolyl unit) appears at 4.83 ppm whereas the four signals at 4.64-4.57 ppm correspond to the glycolyl protons of transesterification sequences that cannot be produced by direct ring opening polymerization. Note that glycolide should lead to sequences having at least two consecutive glycolyl units. Transesterification reactions should mainly occur during the first polymerization step where trimethylene carbonate and ε-caprolactone rings are at the highest ratio.[25] The spectra indicate that the four transesterification sequences (i.e. TGT, TGCap, CapGT and CapGCap listed from downfield to upfield) appeared with similar intensity, and therefore all possible thermally induced transesterification reactions were practically equiprobable. ^{1}H-NMR spectra support an amorphous character of the soft segment due to the multiple sequences produced by practically random copolymerization of the three involved monomers and the occurrence of subsequent transesterification reactions. In fact, the areas of NMR signals indicate that 7.8 molar-% of glycolyl units was incorporated into the transesterification sequences.

The infrared absorption spectrum in the 1800-750 cm^{-1} wavenumber region is highly sensitive to the amorphous and crystalline character of samples, and therefore may be useful to complete their characterization. Figure S3 of SI compares the FTIR spectra of the three homopolymers and the triblock copolymer. The presence of the characteristic bands reported for the crystalline PGL homopolymer,[25,31] indicates that polyglycolide crystalline domains were abundant in the as-processed suture. The spectra changed when the sample was melted and became logically highly similar to that corresponding to amorphous polyglycolide. Despite the low trimethylene carbonate unit content, some typical bands of

amorphous PTMC could still be detected in both amorphous and crystalline copolymer samples.[32] In addition, the presence of crystalline caproyl units can be discarded since their characteristic and well defined bands were not detected.

DSC heating traces of polyglycolide and the triblock copolymers (Figure S4a of SI) showed cleat differences concerning to the melting temperature and enthalpy that logically decreased for the copolymer (i.e. from 213-222 ºC to 200 ºC and from 80 J/g to 40 J/g). The clear decrease on the melting enthalpy corroborated the high amorphous content, being nevertheless the value comparable with that found for the homopolymer when the energy was referred to the hard segment content (i.e. 70 J/g). WAXD diffraction profile of the copolymer (Figure S4b of SI) allowed estimating a degree of crystallinity close to 25%, which was significantly lower than found for PGL and coherent with the hard block content.

Spherulitic morphologies developed during isothermal crystallization of GL-*b*-(GL-*co*-TMC-*co*-CL)-*b*-GL

GL-*b*-(GL-*co*-TMC-*co*-CL)-*b*-GL spherulites were obtained from hot and cold crystallization experiments. In all cases, a positive birefringence was observed (Figure 2) because of the peculiar crystalline structure of polyglycolide. In fact, the structure of polyglycolide is defined by an orthorhombic unit cell with a = 0.522 nm, b = 0.619 nm, and c = 0.702 nm and a $P2_12_12_1$ space group where molecules with a fully extended zigzag conformation form sheets parallel to the *ac* crystallographic plane.[9] The setting angle of the molecular segments is 0º or 180º, values clearly different from typical angles of ±45º determined for other aliphatic polyesters with a planar zigzag conformation. Unlike conventional polyesters that rendered spherulites with a negative birefringence,[33-35] polyglycolide has a perfect alignment of ester groups along the *a* crystallographic

direction. This feature can explain the peculiar positive birefringence when this direction becomes parallel to the spherulitic radi.

Slight differences in spherulitic morphology were detected with the crystallization temperature. Specifically, spherulites grown at the higher temperatures had a flower-like appearance (e.g. crystallization performed at 160 ºC in Figure 2a) characterized by the development of multiple sectors. This morphology may suggest confined crystallization of flat-on lamellae instead of formation of edge-on or even twisted lamellae going round the spherulite, as is characteristic of typical fibrilar or ringed spherulites. Irregular boundaries derived from this morphology were still evident at 145 ºC (arrows in Figure 2b), but perfectly round morphologies formed at even lower temperatures (e.g. Figure 2c for crystallization at 80 ºC). Logically, spherulites obtained from cold crystallization (Figure 2d) showed similar characteristics to those observed at low temperature crystallizations from the melt state. It is also clear that the latter had a fibrilar morphology whereas at the highest temperature greater crystalline domains that could correspond to flat-on lamellae were detected within the spherulites. It is also interesting to note that amorphous domains associated with the soft segments should be inside the spherulites since these covered all the available space when they grew until impingement (Figures 2e and 2f).

The intensity of birefringence of spherulites grown following several isothermal steps decreased at lower temperatures for samples crystallized from the melt (Figure 3a) and the glass state (Figure 3b). Micrographs showed that inner crystalline domains were similar in zones formed at different temperatures, although their size clearly decreased with decreasing temperature. In fact, flat-on crystals with lateral dimensions of up to 1 μm were envisaged in the AFM micrographs of spherulites grown at high temperature (blue arrows in Figure 4a), whereas microcrystals had a more acicular, often even twisted (red arrows), form at lower crystallization temperatures (Figure 4b).

These observations were confirmed by electron diffraction patterns recorded from the different spherulites. Thus, typical polyglycolide *hk*0 diffraction pattern with strong 110 (0.399 nm) and 020 (0.309 nm) reflections were easily obtained from high temperature crystallized spherulites (Figure 5a), whereas this pattern was hardly observed in low temperature crystallized samples. In this case, the intensity of reflections was low (Figure 5b) and even asymmetric patterns (Figure 5c) indicative of lamellar twisting were more frequently recorded. The *hk*0 pattern was always oriented with its *a** reciprocal axis parallel to the spherulite radius, justifying the peculiar positive birefringence sign of the spherulite as above indicated.

Secondary nucleation constant for the isothermal crystallization of GL-*b*-(GL-*co*-TMC-*co*-CL)-*b*-GL

Kinetics of crystallization of GL-*b*-(GL-*co*-TMC-*co*-CL)-*b*-GL from the melt and the glass state was studied by optical microscopy. Spherulite radii grew linearly with time until impingement, as shown in Figure 6a for cold crystallization experiments performed in the temperature range from 60 ºC to 90 ºC. Final radii varied in this case between 28 and 65 μm and logically decreased at higher primary nucleation densities (i.e. at lower crystallization temperatures).

Nucleation was very low at the higher temperatures of crystallization experiments carried out from the melt state where spherulites with diameters larger than 500 μm could be obtained. The number of nuclei slightly varied during isothermal crystallization at a given temperature (not shown) and consequently a deviation from a perfect athermal nucleation was detected. As can be seen in Figure 6b, the temperature evolution of primary nucleation reveals a single exponential dependence. It is remarkable that the number of active nuclei is very low (e.g. 335 nuclei/mm^2 at such a

low temperature as 70 ºC), even lower than that determined for Maxon™ (e.g. 600 nuclei/mm^2 at 80 ºC).[23] Crystallization of GL-*b*-(GL-*co*-TMC-*co*-CL)-*b*-GL seems more hindered because of its higher content in non-crystallizable soft segments (i.e. 43 versus 38 wt-%) with a more statistical monomer distribution (i.e. three as opposed to two components).

Figure 7a is the typical bell-shaped curve that defines the temperature dependence of the crystal growth rate. The low nucleation and growth rate allowed the collection of experimental data over the whole temperature range for crystallizations performed from the melt state. Namely, measurements could be taken even when crystallization began during the cooling run from the melt to the selected temperature due to inability of formed spherulites to collapse.

Crystal growth rates determined from cold crystallization experiments fitted also with the same curve (Figure 7a). Data from these cold crystallization experiments could also be achieved for slightly high temperatures despite some crystallization took place during the heating step. For the sake of completeness, the curve previously reported for Maxon™ is also given in Figure 7a.[23] The GL-*b*-(GL-*co*-TMC-*co*-CL)-*b*-GL plot has significant differences concerning a higher supercooling to initiate crystallization and the shift of the curve to lower temperatures. Namely, a greater difficulty for primary nuclei to begin the crystallization process was detected. It should also be pointed out the higher growth rate determined at the maximum of the curve, which may be related to a lower molecular weight (i.e. M_w of 71,000 g/mol as opposed to the value of 95,000 g/mol reported for Maxon™, [23]).

The crystal growth rate was analyzed by the Lauritzen-Hoffman equation:[36]

$$G = G_0 \exp\left[-U^* / \left(R\left(T_c - T_\infty\right)\right)\right] \times \exp\left[-K_g/\left(T_c\left(\Delta T\right) f\right)\right] \qquad (1)$$

where G_0 is a constant preexponential factor, U^* represents the activation energy characteristic of the transport of crystallizing segments across the liquid–crystal interface, T_∞ is the temperature below which such motion ceases, T_c is the crystallization temperature, R is the gas constant, K_g is the secondary nucleation constant, ΔT is the degree of supercooling measured as $T_m^0 - T_c$, and f is a correction factor accounting for the variation in the bulk melting enthalpy per unit volume with temperature ($f = 2T_c/(T_m^0 + T_c)$).

The Lauritzen-Hoffman plot was fitted with a straight line (r^2 = 0.989) when the "universal" values reported by Suzuki and Kovacs[37] (i.e. U^* = 1500 cal/mol and $T_\infty = T_g$ - 30 K) were used in the calculation. A slight variation was introduced (Figure 7b) to improve the fit (i.e. r^2 = 0.991 using U^* = 1740 cal/mol and $T_\infty = T_g$ - 32 K). Nevertheless, kinetic features at low supercoolings are basically governed by the nucleation term, and consequently crystallization rates could become relatively insensitive to the U^* and T_∞ parameters. The plot was used to estimate a secondary nucleation constant of 2.88×10^5 K^2, which is significantly higher than the value reported for Maxon™[,23] (i.e. 1.82×10^5 K^2) and reveals greater difficulty in the crystal growth process. This is probably so because proper arrangement of hard blocks becomes hindered again at higher contents of non-crystallizable soft segments with a more statistical monomer distribution. Results appear more consistent than those attained from calorimetric analyses since in the case of GL-*b*-(GL-*co*-TMC-*co*-CL)-*b*-GL a lack of proportionality between the overall crystallization rate and the crystal growth rate seems to exist.

Kinetic studies for the non-isothermal crystallization of GL-*b*-(GL-*co*-TMC-*co*-CL)-*b*-GL

Non-isothermal procedures can also be applied to study the temperature dependence of the spherulite growth rate during crystallization from both the melt and the glass states.[38-40] Thus, this rate (G) can be estimated by measuring the change of the spherulite radius (R) with temperature (T) at a constant cooling/heating rate (dT/dt):

$$G = dR/dt = (dR/dT)\,(dT/dt) \qquad (2)$$

The plot of the radius versus experimental temperature data can be adjusted to a polynomial equation with a good regression coefficient (r) to calculate the value of its first derivative (dR/dT) as a function of the crystallization temperature for all cooling/heating rates. Experimental problems lie in the choice of the cooling/heating rate required to maximize the crystallization temperature range where radii can be well measured. To this end, the use of various rates can be highly effective.

The change in the radius of a typical GL-*b*-(GL-*co*-TMC-*co*-CL)-*b*-GL spherulite during the temperature ramp at different cooling/heating rates is shown in Figure 8a. A polynomial fitting with a high regression coefficient was obtained in all crystallizations. Third-order equations were always chosen (Table S2 in SI) since regression coefficients ($\geq$ 0.979) were slightly better than those calculated for lower order equations and remained constant for higher orders.

Relationships between spherulite growth rate and crystallization temperature were obtained by differentiating third-order equations based on temperature and considering the cooling/heating rate (Equation 2). Figure 8b plots the G values, deduced for several cooling/heating rates as a function of temperature. A bell-shaped curve with a maximum of 122 ºC was derived with data from all crystallization temperatures. It is remarkable that spherulite growth rates could be measured in the low temperature range (48-117 ºC) from crystallization experiments from both the glass and the melt state. Relatively good

agreement was found between data obtained from isothermal and non-isothermal crystallization, as also shown in Figure 8b.

Lauritzen-Hoffman equation 1 was also used to deduce the value of the secondary nucleation constant for non-isothermal crystallization. Figure 8c shows the linear plot obtained using U^* and T_∞ parameters of 1780 cal/mol and T_g – 33 K, respectively. It is clear that a single crystallization regime defined by a secondary nucleation constant of 2.42×10^5 K^2 fits all the experimental data. The good agreement between experimental and theoretical data (i.e. those obtained from equation 1 and the deduced parameters) is also shown in Figure 8b. The deduced secondary nucleation constant is similar to, although slightly lower than, that determined from isothermal analysis (i.e. 2.42×10^5 K^2 respect to 2.88×10^5 K^2). Note that the average constant (2.65×10^5 K^2) is clearly higher than the value determined from DSC experiments and becomes higher than the average constant deduced from isothermal and non-isothermal crystallizations of the GL-*b*-(GL-*co*-TMC)-*b*-GL bicomponent system (2.13×10^5 K^2).[24] Therefore, analyses from optical microscopy observations render reliable values of the secondary nucleation constant that justify a greater difficulty to crystallize for samples having a more disordered soft segment despite having a lower molecular weight.

Changes on lamellar morphology of GL-*b*-(GL-*co*-TMC-*co*-CL)-*b*-GL during cooling and heating processes

Figure 9a shows representative time-resolved SAXS profiles of GL-*b*-(GL-*co*-TMC-*co*-CL)-*b*-GL obtained during a non-isothermal hot crystallization performed at 10 ºC/min. A SAXS long period peak is clearly seen at a value of the scattering vector, $q = [4\pi/\lambda] \sin(\theta)$, close to 0.45 nm^{-1} after substraction of the empty sample background observed near the beam stop. This peak can be attributed to the lamellar structure of the

spherulites and starts to appear at a temperature close to 147 ºC (a value which slightly increases with decreasing the crystallization cooling rate). Subsequently, the peak intensity increases significantly with decreasing temperature until reaching a plateau value at a temperature close to 126 ºC at which crystallization can be considered completely finished. The high intensity of the final SAXS peaks, suggests a large difference between the electronic density of the amorphous and the crystalline phases, which is in agreement with the tight packing of polyglycolide.[9] During crystallization the SAXS peak slightly shifts to higher q values and the change is more pronounced at the initial stages.

Characteristic lamellar parameters (i.e. long period, L_γ, amorphous layer thickness, l_a, and crystalline lamellar thickness, l_c) and crystallinity (i.e. crystallinity within the lamellar stacks, $X_c^{SAXS} = l_c / L_\gamma$, and scattering invariant, Q) were determined by means of the normalized one-dimensional correlation function,[41] $\gamma(r)$:

$$\gamma(r) = \int_0^\infty q^2 I(q) \cos(qr) dq \; / \; \int_0^\infty q^2 I(q) dq \qquad (3)$$

SAXS data were collected within a limited angular range and consequently Vonk's model[42] and Porod's law were applied to perform extrapolations to low and high q values.

Representative correlation functions (i.e. at the beginning and at the end of the crystallization process) are displayed in Figure 10 whereas the evolution of morphologic parameter and the invariant are shown in Figure 11. Main conclusions that can be deduced for the crystallization process are the followings: a) L_γ was clearly higher than the long period determined from twice the value of the first minimum of the correlation function (i.e. 10.6 nm respect to 8.0 nm), which suggests a broad distribution of the layer widths of the crystal phase. b) l_a remained practically constant during

crystallization since only a decrease from 2.2 to 1.9 nm was detected, whereas l_c significantly decreased (i.e. from 9.8 to 8.6 nm) as a consequence of a typical lamellar insertion mechanism. c) Scattering invariant logically increased during non-isothermal crystallization but at low temperature (e.g. close to 51 ºC) it starts to decrease as a consequence of an increase on the electronic density of the interlamellar amorphous phase. d) Crystallinity within the lamellar stacks was very high (0.82) as a consequence of the reduced amorphous thickness. In fact, this is a distinctive feature with respect to Maxon™ samples crystallized under identical experimental conditions and a clear evidence of the influence of microstructure on morphology. In the case of Maxon™ the final l_a and l_c parameters were 10.0 and 3.5 nm, respectively, whereas X_c^{SAXS} was only 0.74.

Lamellar structure is clearly different for the as-processed sutures, which display a typical fiber pattern with oriented WAXD reflections (not shown) and an intense meridional SAXS reflection (Figure 10). Lamellar structure is defined by l_a and l_c parameters of 5.1 and 1.3 nm, respectively, and a X_c^{SAXS} value of 0.80. Thus, processing characterized by a rapid cooling from spinneret and a subsequent annealing process render a well differentiated structure from melt crystallized spherulites as can be deduced by comparison of correlation functions (Figures 10a and 10c). Again a broad distribution of the layer widths of the crystal phase can be deduced for the as processed sample (i.e. 6.3 nm and 4.8 nm are measured for the first maximum and the double value of the first minima, respectively). Despite the great difference on the lamellar morphology it should be indicated that X_c^{SAXS} was very close to the value determined for melt crystallization (i.e. 0.80 with respect to 0.82). Morphology drastically changed during a subsequent heating process since the SAXS peak increased in intensity (probably as consequence of the decrease of the electronic density of the interlamellar

amorphous phase) and moved towards lower q values (Figure 9b). This lamellar reordering process was initiated at a temperature close to 101 ºC and ended at 202 ºC just when melting process began. It should be pointed out that any endothermic event was observed in previous DSC experiments[28] and consequently diffraction data are essential to demonstrate the thickening process of GL-*b*-(GL-*co*-TMC-*co*-CL)-*b*-GL. Figures 10b and 11 shows the correlation function at the end of lamellar reordering process and the temperature evolution of morphologic parameters. Note that they were practically constant up to 115 ºC, increased between 115 and 190 ºC and decreased at higher temperatures than 190 ºC. The evolution of the amorphous and crystalline lamellar thicknesses was proportional and consequently X_c^{SAXS} remained practically constant (increased only from 0.80 to 0.82). It is remarkable that the lamellar structure became practically identical to that attained after crystallization from the melt (Figures 12b and 12d), being l_a and l_c parameters 9.0 and 2.0 nm, respectively (i.e. close to the previously reported values of 8.6 and 1.9 nm).

CONCLUSIONS

Crystallization of segmented copolymers having two polyglycolide hard segments is influenced by the constitution of the middle amorphous soft segment. Specifically, significant differences on secondary nucleation constant and lamellar morphology were found between copolymers displaying similar properties but having soft segments with three (i.e. glycolide, trimethylene carbonate and ε-caprolactone) or two components (i.e. glycolide and trimethylene carbonate). Results from isothermal and non-isothermal crystallization experiments were consistent and pointed out that the statistical segments constituted by three repeat units hindered the proper arrangement of hard blocks over

crystal surfaces, being also detected a clear decrease on the primary nucleation respect the related bicomponent copolymer.

Similar lamellar morphologies were attained by crystallization from the melt state or from thermal treatment of oriented fibers, being characteristic lamellar insertion and lamellar thickening processes, respectively. Final morphologies were defined by a crystallinity within the lamellar stacks of 0.82 and a crystalline thickness of 8.6-9.0 nm that contrast with values of 0.74-0.83 and 10.0 nm found for the bicomponent system when was processed in a similar form.

Acknowledgements. Authors are in debt to supports from MINECO and FEDER (MAT2012-36205) and the Generalitat de Catalunya (2014SGR188). The work has also been carried out under a research agreement between B. Braun Surgical, S. A. and the Universitat Politècnica de Catalunya. Ms Y. Márquez thanks finantial support from B. BRAUN Surgical S.A. Diffraction experiments were performed at NCD beamline at ALBA Synchrotron with the collaboration of ALBA staff.

REFERENCES

1. Schmitt EE, Polistina RA. Surgical sutures. U.S. Patent 3.297.033. American Cyanamid 1967.
2. Schmitt EE, Polistina RA. Polyglycolic acid prosthetic devices. U.S. Patent 3.463.158. American Cyanamid 1969.
3. Cameron RE, Kamvari-Moghadam A. Synthetic bioresorbable polymers. Durability and reliability of medical polymers 2012. p. 96–118.
4. Pillai CKS, Sharma CP. Review paper: absorbable polymeric surgical sutures: chemistry, production, properties, biodegradability, and performance. J Biomater Appl 2010;25(4):291–366.
5. Kundra RK, Newman S, Saithna A, Lewis AC, Srinivasan S, Srinivasan K. Absorbable or non-absorbable sutures? A prospective, randomised evaluation of aesthetic outcomes in patients undergoing elective day-case hand and wrist surgery. Ann R Coll Surg Engl 2010;92(8):665–7.
6. Nair LS, Laurencin CT. Biodegradable polymers as biomaterials. Prog Polym Sci 2007;32(8-9):762–98.
7. Ulery BD, Nair LS, Laurencin CT. Biomedical applications of biodegradable polymers. J Polym Sci B Polym Phys 2011;49(12):832–64.
8. Gunatillake P, Mayadunne R, Adhikari R. Recent developments in biodegradable synthetic polymers. Biotechnol Annu Rev 2006;12:301–47.
9. Chatani Y, Suehiro K, Okita Y, Tadokoro H, Chujo K. Structural studies of polyesters. I Crystal structure of polyglycolide. Die Makrornolekulare Chemie 1968;113(2687):215–29.

10. Brandrup J, Immergut EH, Grulke EA. Solid State Properties. Polymer Handbook. 4th ed. New York: Interscience Publishers; 1999.
11. Farrar D. Modelling of the degradation process of bioresorbable polymers. Durability and reliability of medical polymer 2008. p. 186–206.
12. Noorsal K, Mantle MD, Gladden LF, Cameron RE. Degradation and drug-release studies of a poly(glycolide-co-trimethylene carbonate) copolymer (Maxon). J Appl Polym Sci 2005;95(3):475–86.
13. Freudenberg S, Rewerk S, Kaess M, Weiss C, Dorn-Beinecke A, Post S. Biodegradation of absorbable sutures in body fluids and pH buffers. Eur Surg Res 2004;36:376–85.
14. Sun L, Wanasekara N, Chalivendra V, Calvert P. Nano-mechanical studies on polyglactin sutures subjected to in vitro hydrolytic and enzymatic degradation. J Nanosci Nanotechnol 2005;15(1):93–9.
15. Haghighat F, Ravandi SAH. Mechanical properties and in vitro degradation of PLGA suture manufactured via electrospinning. Fibers Polym 2014;15(1):71–7.
16. Homsy CA, Mcdonald ER, Akers WW. Surgical suture-canine tissue tnteraction for six common suture types. J Biomed Mater Res 1968;2:215–30.
17. Blomstedt B, Ostenberg B. Suture materials and wound infection. An experimental study. Acta Chir Scand 1978;144:269–74.
18. Rodeheaver GT, Ph D, Thacker JG, Owen J, Edlich RF. Knotting and handling characteristics of coated synthetic absorbable sutures. J Surg Res 1983;35:525–30.
19. Katz AR, Mukherjee DP, Kaganov AL, Gordon S. A new synthetic monofilament absorbable suture made from polytrimethylene carbonate. Surgery, Gynecol Obstet 1985;161:213–22.

20. Oberhoffner S, Planck H. Surgical suture material from triblockterpolymer, its use in surgery and process for its preparation. EP 0835895. 1996.
21. Roby MS, Bennet SL, Liu EK. Absorbable block copolymers and surgical articles fabricated thereform. U.S.Patent 5.403.347. 1995.
22. Bezwada RS, Jamiolkowski DD, Lee I, Persivale J, Trenka-Benthin S, Emeta M, et al. Monocryl® suture, a new ultra-pliable absorbable monofilament suture. Biomaterials 1995;16(15):1141–8.
23. Díaz-Celorio E, Franco L, Puiggalí J. Isothermal crystallization study on a biodegradable segmented copolymer constituted by glycolide and trimethylene carbonate units. J Appl Polym Sci 2010;116:577–89.
24. Díaz-Celorio E, Franco L, Puiggalí J. Nonisothermal crystallization behavior of a biodegradable segmented copolymer constituted by glycolide and trimethylene carbonate units. J Appl Polym Sci 2011;119:1548–59.
25. Díaz-Celorio E, Franco L, Rodríguez-Galán A, Puiggalí J. Synthesis of glycolide/trimethylene carbonate copolymers: Influence of microstructure on properties. Eur Polym J 2012;48(1):60–73.
26. Díaz-Celorio E, Franco L, Rodríguez-Galán A, Puiggalí J. Study on the hydrolytic degradation of glycolide/trimethylene carbonate copolymers having different microstructure and composition. Polym Degrad Stab 2013;98(1):133–43.
27. Díaz-Celorio E, Franco L, Puiggalí J. Influence of microstructure on the crystallization of segmented copolymers constituted by glycolide and trimethylene carbonate units. Express Polym Lett 2013;7(2):186–98.
28. Márquez Y, Franco L, Turon P, Puiggalí J. Isothermal and non-isothermal crystallization kinetics of a polyglycolide copolymer having a tricomponent middle soft segment. Thermochim Acta 2014;585:71–80.

29. Zurita R, Puiggalí J, Franco L, Rodríguez-Galán A. Copolymerization of glycolide and trimethylene carbonate. J Polym Sci Part A Polym Chem 2005;44(2):993–1013.

30. Kasperczyk J. Copolymerization of glycolide and e-caprolactone , 1 Analysis of the copolymer microstructure by means of 1H and 13C NMR spectroscopy. Macromol Chem Phys 1999;910(4):903–10.

31. Kister G, Cassanas G, Vert M. Morphology of poly (glycolic acid) by IR and Raman spectroscopies. Spectrochim Acta Part A 1997;53:1399–403.

32. Wang H, Dong J, Qiu K. Synthesis and characterization of ABA-type block copolymer of poly (trimethylene carbonate) with poly (ethylene glycol): Bioerodible Copolymer. J Polym Sci Part A Polym Chem 1998;36:695–702.

33. Xu J, Guo BH, Zhou JJ, Li L, Wu J, Kowalczuk M. Observation of banded spherulites in pure poly(L-lactide) and its miscible blends with amorphous polymers. Polymer 2005;46:9176-9185.

34. Nikolova L, Ramanujam PS. Azobenzene and azobenzene-containing polymers (Chapter 4) Polarization Holography. 1st ed. UK: Cambridge University Press; 2009;

35. Magill JH. Review Spherulites: A personal perspective, J. Mater. Sci 2001;36:3134-3164)

36. Lauritzen JI. Extension of theory of growth of chain-folded polymer crystals to large undercoolings. J Appl Phys 1973;44(10):4340.

37. Suzuki T, Kovacs AJ. Temperature dependence of spherulitic growth rate of isotactic polystryrene. A critical comparison with the kinetic theory of surface nucleation. Polym J 1970;1:82–100.

38. Chen M, Chung C. Analysis of crystallization kinetics of poly (ether ether ketone) by a nonisothermal method. J Polym Sci Part B Polym Phys 1998;36:2393–9.

39. Di Lorenzo ML, Cimmino S, Silvestre C. Nonisothermal crystallization of isotactic polypropylene blended with poly (α-pinene). 2 . Growth Rates. Macromolecules 2000;33:3828–32.
40. Di Lorenzo LM. Determination of spherulite growth rates of poly (l-lactic acid) using combined isothermal and non-isothermal procedures. Polymer 2001;42:9441–6.
41. Vonk CG, Kortleve G. X-Ray Small-Angle Scattering of bulk polyethylene. Kolloid Z Z Polym 1967;220:19–24.
42. Vonk CG. A general computer program for the processing of small-angle X-ray scattering data. J Appl Crystallogr 1975;8:340–1.

FIGURE CAPTIONS

Figure 1. ^{1}H-NMR spectra of GL-*b*-(GL-*co*-TMC-*co*-CL)-*b*-GL with labelling of the most distinctive sequences. Inset shows a detail of glycolyl signals and characteristic transesterification sequences.

Figure 2. Polarized optical micrographs of GL-*b*-(GL-*co*-TMC-*co*-CL)-*b*-GL spherulites crystallized from the melt (a, b, c, e) and cold crystallized (d, f). Black and white micrographs correspond to samples crystallized at 160 ºC (a), 145 ºC (b), 80 ºC (c), 70 ºC (d), whereas color micrographs were taken at the end of crystallizations performed at 155 ºC (e) and 70 ºC (f) using a first-order red tint plate. Arrows point to irregular edges detected during high temperature crystallizations.

Figure 3. Polarized optical micrographs of GL-*b*- (GL-*co*-TMC-*co*-CL)-*b*-GL spherulites isothermally grown at three temperatures starting at 150 ºC (a) and 85 ºC (b).

Figure 4. Atomic force microscopy 3D height images of GL-*b*-(GL-*co*-TMC-*co*-CL)-*b*-GL spherulites isothermally crystallized from the melt and the glass state at 150 ºC (a) and 80 ºC (b), respectively. Insets show amplitude and low magnification 3D height images.

Figure 5. Electron diffraction patterns of GL-*b*-(GL-*co*-TMC-*co*-CL)-*b*-GL spherulites crystallized from the melt and the glass state at 150 ºC (a) and 80 ºC (b,c), respectively. In all cases, the a^* reciprocal axis is parallel to the spherulite radius.

Figure 6. a) Plots of the radius of GL-*b*-(GL-*co*-TMC-*co*-CL)-*b*-GL spherulites versus crystallization time for isothermal cold crystallizations performed between 60-90 ºC. b) Change in the nucleation density with isothermal crystallization temperature.

Figure 7. a) Temperature dependence of crystal growth rate (○ symbols) determined by equation 1 and using the best fit parameters. Experimental crystal growth rates (green and red symbols for crystallizations from the glass and the melt state, respectively) as well as the theoretical curve from isothermic crystallization of GL-*b*-(GL-*co*-TMC)-*b*-GL (□ symbols)[13] are also shown for comparison. b) Plot of ln $G + U^* / R(T_c-T_\infty)$ versus $1/T_c(\Delta T)\, f$ to determine the K_g secondary nucleation parameter of GL-*b*-(GL-*co*-TMC-*co*-CL)-*b*-GL.

Figure 8. a) Variation in spherulite radius with temperature during heating and cooling at the indicated rates. b) Spherulite growth rates determined by the equations deduced for cooling and heating runs. Theoretical curves for non-isothermal (○) and isothermal (-) crystallization of GL-*b*-(GL-*co*-TMC-*co*-CL)-*b*-GL are also drawn for comparative purposes. For the sake of completeness, insets show representative spherulites non-isothermally crystallized from the melt and the glass state that had irregular and rounded edges, respectively. c) Plot of ln $G + U^* / R(T_c-T_\infty)$ versus $1 / T_c(\Delta T)\, f$ to determine the K_g secondary nucleation parameter of GL-*b*-(GL-*co*-TMC-*co*-CL)-*b*-GL.

Figure 9. Time-resolved SAXS three-dimensional profiles of GL-*b*-(GL-*co*-TMC-*co*-CL)-*b*-GL during non-isothermal crystallization from the melt (a) and heating from room temperature (b). Heating and cooling rates were 10 ºC/min. SAXS curves are shown after subtraction of empty sample background and Lorentz correction.

Figure 10. Comparison between correlation functions of GL-*b*-(GL-*co*-TMC-*co*-CL)-*b*-GL for: initial sample (a), after heating up to 180 ºC (b), at the first stages of crystallization from the melt (c) and after finishing the non-isothermal crystallization (d). Heating and cooling rates were 10 ºC/min.

Figure 11. Evolution of the long period from correlation function (●), L_γ, crystal thickness (■), l_c, amorphous thickness (▲), l_a, and scattering invariant (♦), Q, during non-isothermal crystallization performed at 10 ºC/min with GL-*b*-(GL-*co*-TMC-*co*-CL)-*b*-GL sample. Evolution of spacing parameters during a heating scan (10 ºC/min) of the initial sample is also shown (empty symbols).

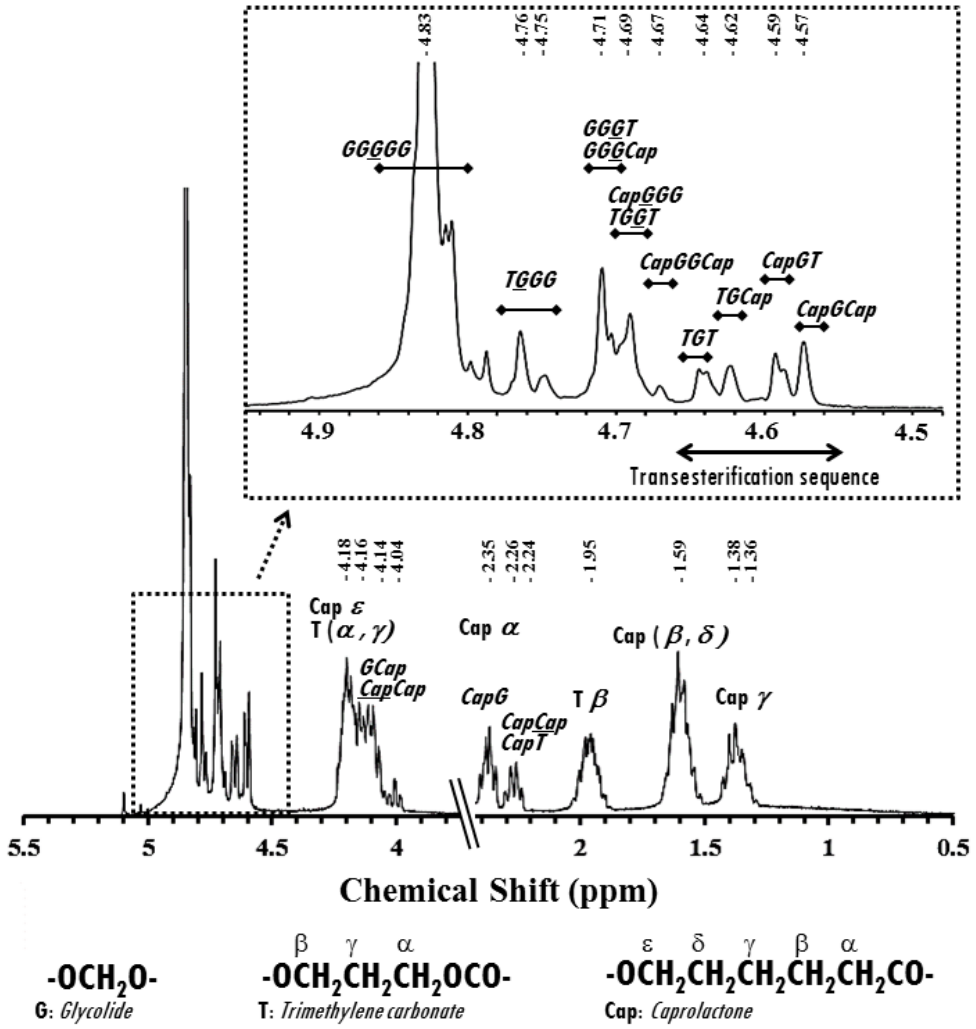

Figure 1

Márquez *et al.*

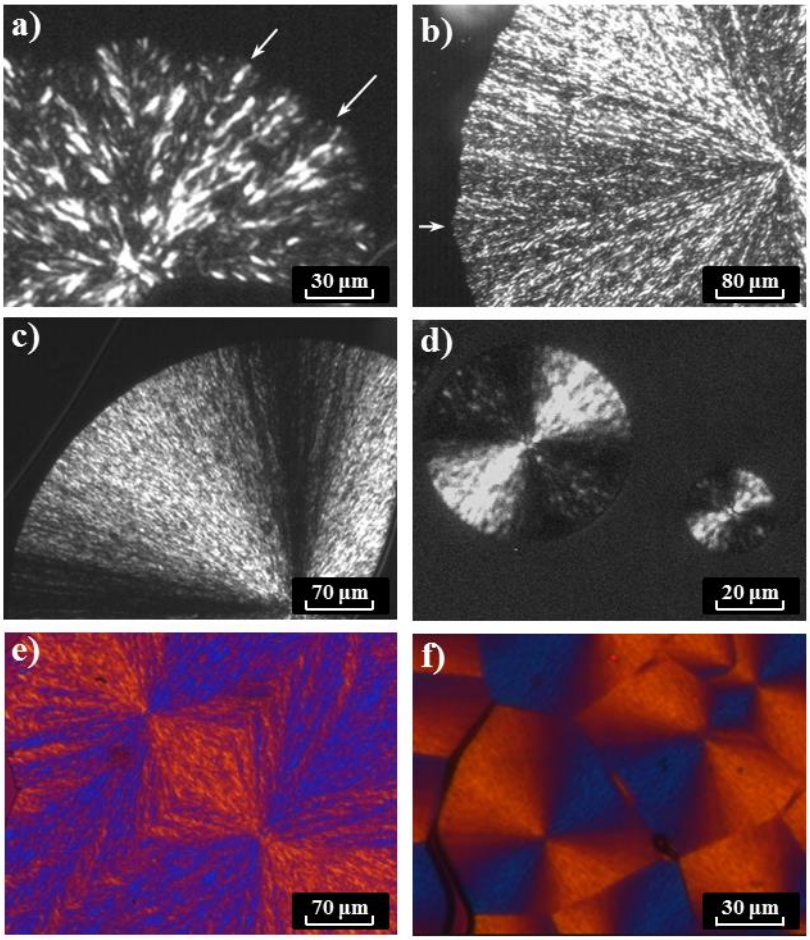

Figure 2

Márquez *et al.*

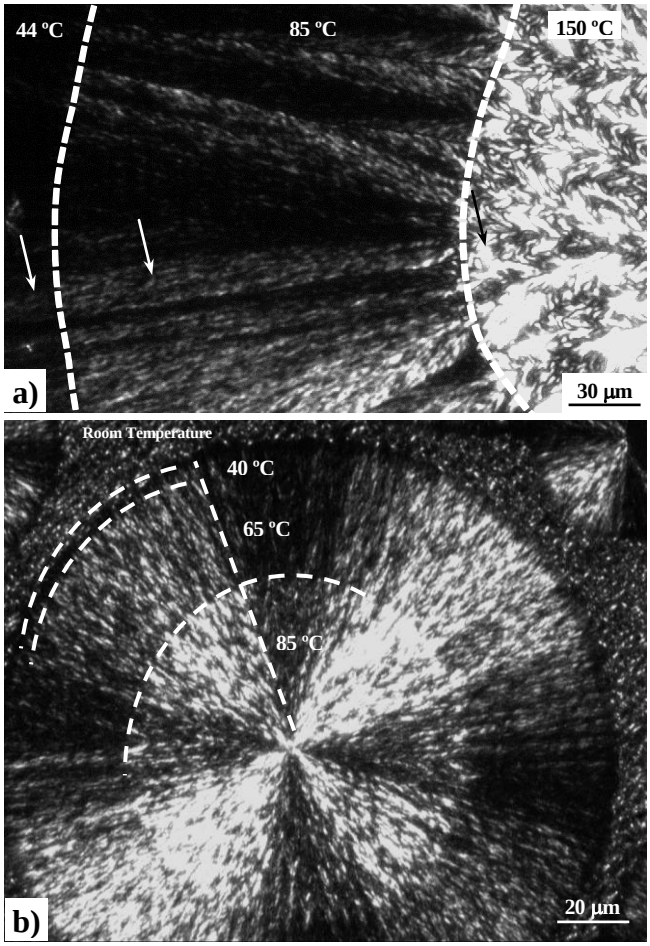

Figure 3

Márquez *et al.*

Eliminar el detalle de a) el rectángulo superior y también el recuadro punteado en a)

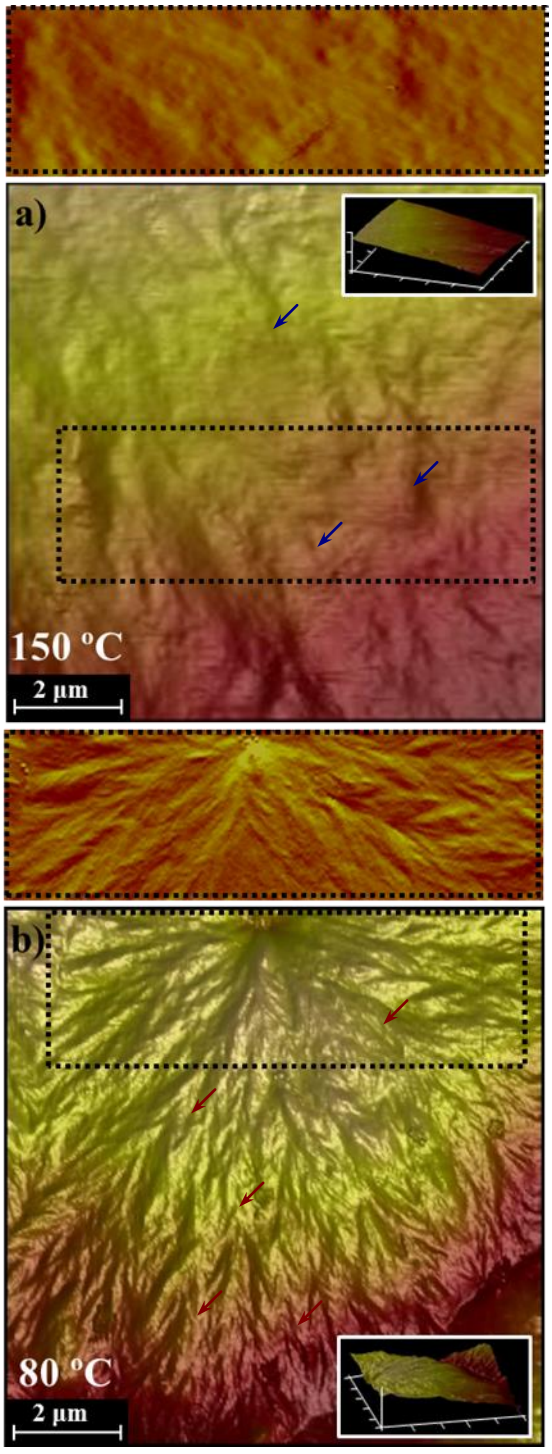

Figure 4

Márquez *et al.*

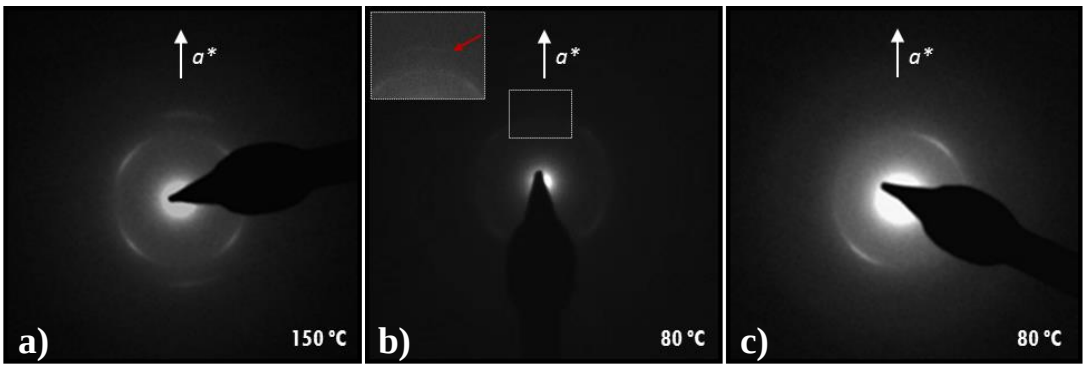

Figure 5

Márquez *et al.*

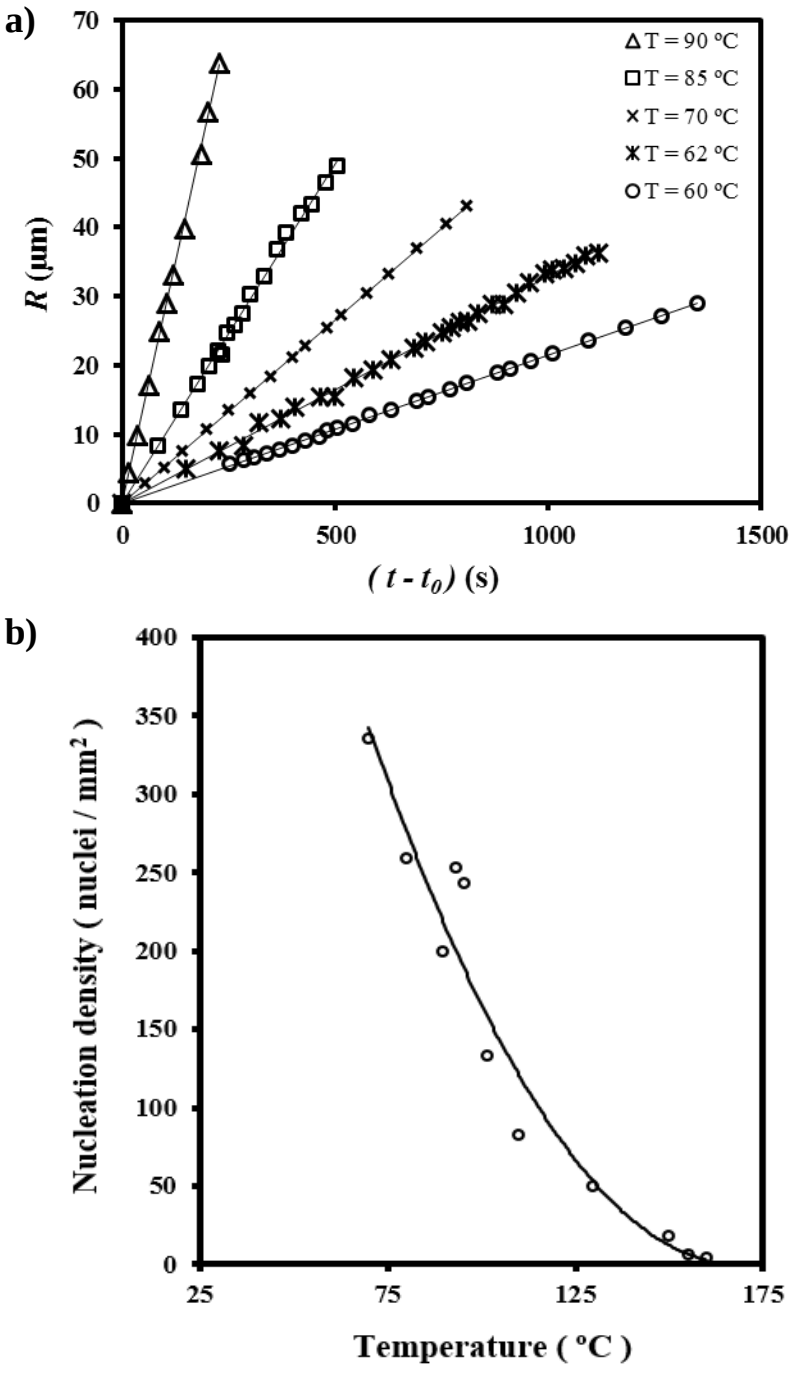

Figure 6

Márquez *et al.*

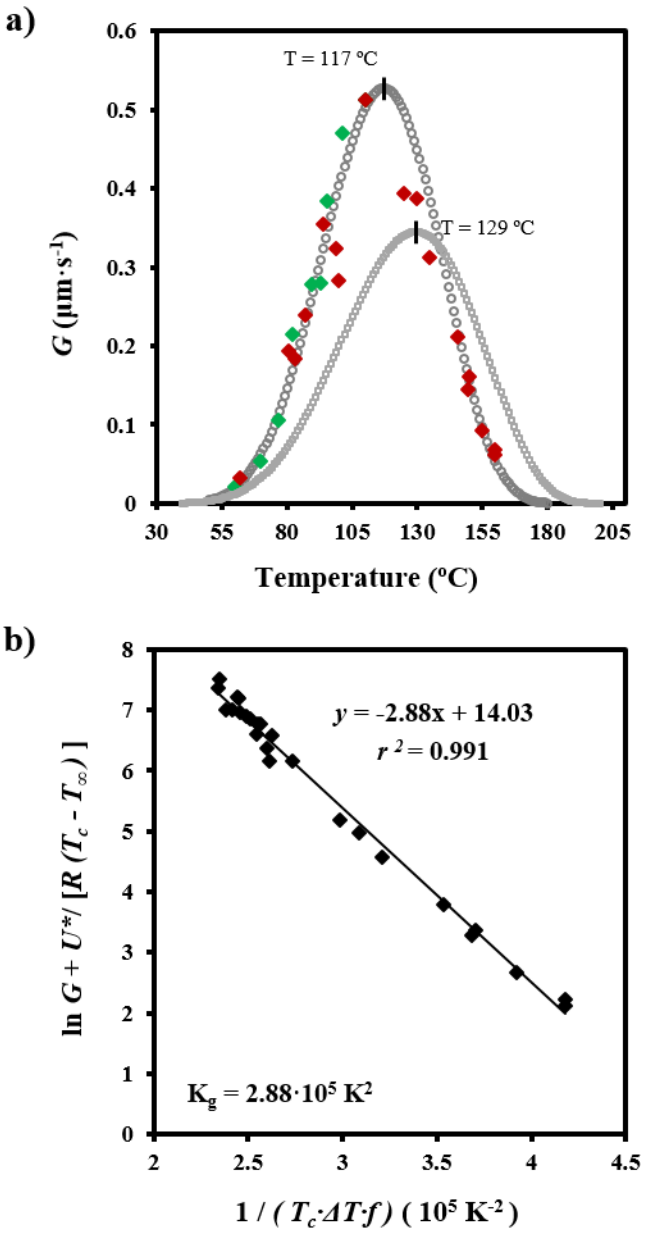

Figure 7

Márquez *et al.*

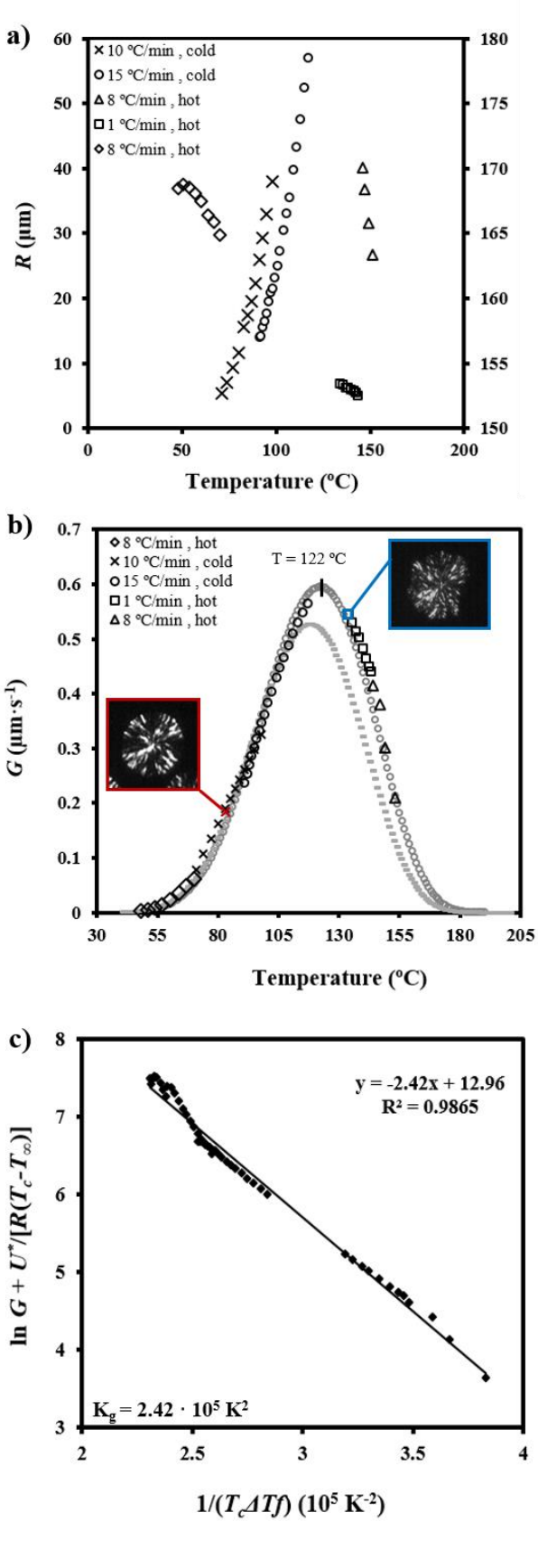

Figure 8

Márquez *et al.*

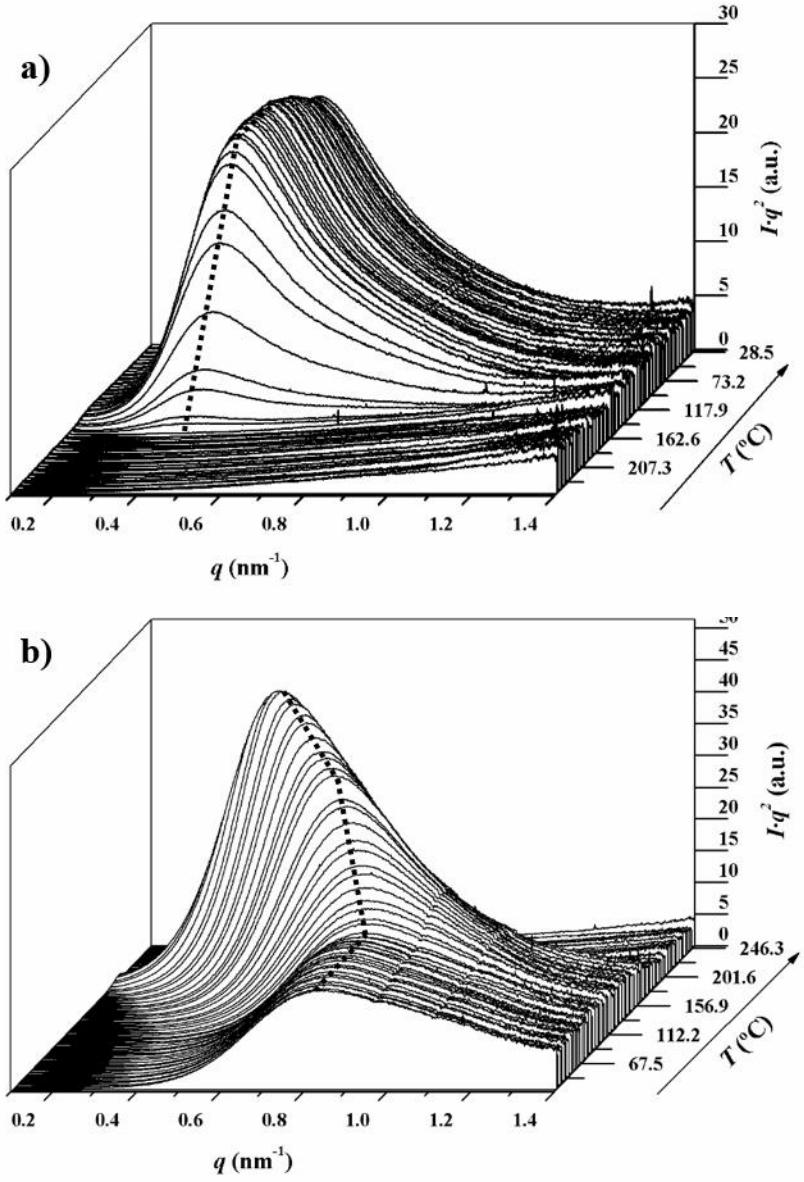

Figure 9

Márquez *et al.*

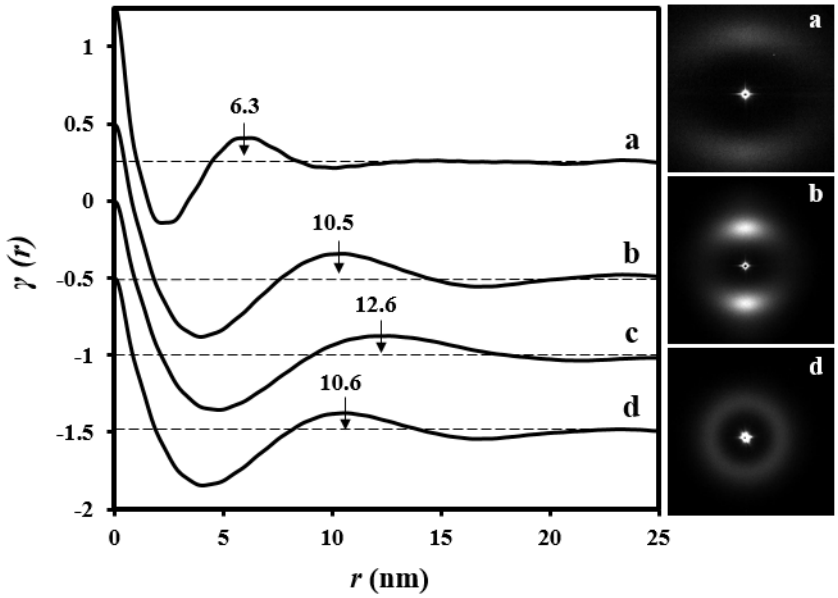

Figure 10

Márquez *et al.*

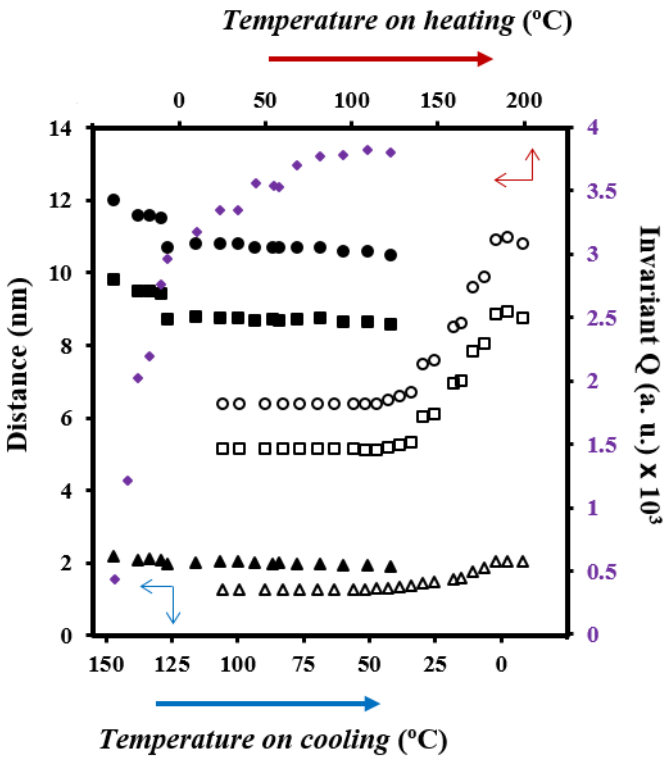

Figure 11

Márquez *et al.*